MNRAS **000**, 1–12 (2018) Preprint 13 August 2018 Compiled using MNRAS LATEX style file v3.0

The *Kepler* Smear Campaign I: An Asteroseismic Catalogue of Bright Red Giants

Benjamin J. S. Pope,[1,2,3]★ Guy R. Davies,[4,5] Keith Hawkins,[6,7] Timothy R. White,[5,8] Daniel Huber,[9,10,11] Ashley Chontos,[9] Victor Silva Aguirre,[5] Victoria Antoci,[5] Suzanne Aigrain,[3] Timothy R. Bedding,[10,5] Jie Yu,[10,5] Amalie Stokholm,[5] and friends

[1]*Center for Cosmology and Particle Physics, Department of Physics, New York University, 726 Broadway, New York, NY 10003, USA*
[2]*NASA Sagan Fellow*
[3]*Oxford Astrophysics, Denys Wilkinson Building, University of Oxford, OX1 3RH, Oxford, UK*
[4]*School of Physics and Astronomy, University of Birmingham, Birmingham B15 2TT, UK*
[5]*Stellar Astrophysics Centre, Department of Physics and Astronomy, Aarhus University, Ny Munkegade 120, DK-8000 Aarhus C, Denmark*
[6]*Department of Astronomy, The University of Texas at Austin, 2515 Speedway Boulevard, Austin, TX 78712, USA*
[7]*Department of Astronomy, Columbia University, 550 W 120th St, New York, NY 10027, USA*
[8]*Research School of Astronomy and Astrophysics, Mount Stromlo Observatory, The Australian National University, Canberra, ACT 2611, Australia*
[9]*Institute for Astronomy, University of HawaiâĂŸi, 2680 Woodlawn Drive, Honolulu, HI 96822, USA*
[10]*Sydney Institute for Astronomy (SIfA), School of Physics, University of Sydney, NSW 2006, Australia*
[11]*SETI Institute, 189 Bernardo Avenue, Mountain View, CA 94043, USA*

Accepted XXX. Received YYY; in original form ZZZ

ABSTRACT

Here we present the first data release of the *Kepler* Smear Campaign, using collateral 'smear' data obtained by *Kepler* to reconstruct light curves of 102 stars too bright to have been otherwise observed. We describe the pipeline developed to extract and calibrate these light curves, and show that we attain photometric precision comparable to stars observed ordinarily in the nominal *Kepler* mission. In this Paper, we focus in particular on a subset of these consisting of 64 red giants for which we detect solar-like oscillations. Using high-resolution spectroscopy from the Tillinghast Reflector Échelle Spectrograph (TRES) together with asteroseismic modelling, we obtain the masses and evolutionary states of 27 of these red giant and red clump stars as benchmarks. All source code, light curves, TRES spectra, and asteroseismic and stellar parameters are publicly available as a *Kepler* legacy sample.

Key words: asteroseismology – techniques: photometric – stars: variable: general

1 INTRODUCTION

The *Kepler* Space Telescope, operated by NASA, was launched in 2009 to obtain photometry of hundreds of thousands of stars in a field in Cygnus-Lyra, in order to detect a statistically-useful sample of transiting exoplanets (Borucki et al. 2010). It achieved this primary goal, showing that exoplanets are common around Sun-like stars (Fressin et al. 2013; Petigura et al. 2013; Foreman-Mackey et al. 2014), though with the failure of two reaction wheels, the mission was cut short and there remain substantial uncertainties on these estimates. *Kepler* was revived as a two-wheeled mission, K2, with its third axis balanced against solar radiation pressure. K2 is therefore constrained to point in the ecliptic plane, which it surveys in a succession of ∼ 80 day Campaigns. In this paper, we will deal exclusively with data from the nominal *Kepler* mission before this change.

Beyond searching for planets, *Kepler* has revolutionized the field of asteroseismology (Gilliland et al. 2010). It has yielded the first detection of gravity-mode period spacings in a red giant (Beck et al. 2011), enabling probes of interior rotation of red giants (Beck et al. 2012) and distinguishing between hydrogen- and helium-burning cores (Bedding et al. 2011). It has also permitted the determination of ages and fundamental parameters of main-sequence stars (Silva Aguirre et al. 2013), including planet-hosting stars (Huber et al. 2013; Silva Aguirre et al. 2015; Van Eylen et al. 2018), revealing the most ancient known planetary system, dating back to the earliest stages of the galaxy (Campante et al. 2015). By comparing asteroseismic stellar ages to stellar rotation periods, Angus et al. (2015) have shown that gyrochronology models cannot fit the data with a single relation, leading van Saders et al. (2016)

★ E-mail: benjamin.pope@nyu.edu

© 2018 The Authors

to suggest a qualitative change in dynamo mechanism as stars age through the main sequence.

A major outcome of the *Kepler* asteroseismology programme is a legacy sample of extremely well characterized stars which can serve as benchmarks for future work (Lund et al. 2016; Silva Aguirre et al. 2016). As well as asteroseismology, by also using optical interferometry, it has been possible to determine fundamental parameters of main-sequence and giant stars with unprecedented precision (Huber et al. 2012; White et al. 2013, 2015). Likewise by combining with spectroscopy, Hawkins et al. (2016c) have been able to produce a large sample of stars with precise elemental abundances by fitting spectroscopic data with $\log g$ and $T_{\rm eff}$ fixed to asteroseismically-determined values. It is necessary to calibrate such a study against benchmark stars with very precisely-determined parameters, which in practice means requires nearby bright stars that are amenable to very high signal-to-noise spectroscopy plus asteroseismology (Creevey et al. 2013), parallaxes (Hawkins et al. 2016a), and/or interferometry (Casagrande et al. 2014; Creevey et al. 2015). This is especially important in the context of the *Gaia* mission (Gaia Collaboration et al. 2016), which has recently put out its second data release of 1,692,919,135 sources, including 1,331,909,727 with parallaxes (Gaia Collaboration et al. 2018). These data will form the basis of many large surveys and it is vital that they are calibrated correctly. To this end, 34 FGK stars have been chosen as *Gaia*-ESO benchmark stars for which metallicities (Jofré et al. 2014), effective temperatures and surface gravities (Heiter et al. 2015), and relative abundances of α and iron-peak elements (Jofré et al. 2015) have been determined. This has been accompanied by the release of high resolution spectra (Blanco-Cuaresma et al. 2014) and formed the basis of extensions to lower metallicities (Hawkins et al. 2016b), stellar twin studies (Jofré 2016) and comparisons of stellar abundance determination pipelines (Jofré et al. 2017).

Brighter *Kepler* stars are therefore ideal benchmark targets, as photometry can be most easily complemented by *Hipparcos* parallaxes, interferometric diameters, and high resolution spectroscopy. Unfortunately, the *Kepler* field was deliberately placed to minimize overall the number of saturated stars, so that only a dozen stars brighter than 6th magnitude landed on silicon (Koch et al. 2010). This was because stars brighter than $Kp \sim 11$ saturate the CCD detector, spilling electrons up and down their column on the CCD and rendering these pixels otherwise unusable. Furthermore, due to the limited availablility of bandwidth to download data from the satellite, only a fraction What fraction? of pixels on the *Kepler* detector are actually downloaded, these being allocated via a competitive proposal process. The result of these two target selection constraints is that photometry was obtained for only a small number of saturated stars in the *Kepler* field, while many bright targets were ignored.

Kolodziejczak & Caldwell (2011) noted that there is a way to obtain photometry of every target on-silicon in *Kepler* using a data channel normally used for calibration, even if active pixels were not allocated and downloaded. *Kepler* employs an inter-line transfer CCD as its detector, which successively shuffles each row of pixels down to the edges of the chip where they are ultimately read out. Because the *Kepler* camera lacks a shutter, the detector is exposed to light during the readout process, with the result that fluxes in each pixel are biased up by light collected from objects in the same column. This is a particularly serious issue for faint objects in the same detector column as brighter stars, and it is important to calibrate this at each readout stage. Six rows of blank 'masked' pixels are allocated in each column to measure the smear bias; furthermore, six 'virtual' rows are recorded at the end of the readout, with the result that twelve rows of pixels sample the smear bias in each column. Kolodziejczak & Caldwell (2011) realized that these encode the light curves of bright targets in a 1D projection of the star field. The masked and virtual smear registers each receive $\sim 1/1034$ of the incident flux in each column; if this is dominated by the light from a single star, the flux combining both smear registers is equivalent to that of a star ~ 6.8 times fainter.

In Pope et al. (2016), we demonstrated a method for extracting precise light curves of bright stars in *Kepler* and K2, and presented light curves of a small number of variable stars as examples to illustrate this method. In this Paper we present light curves of all unobserved or significantly under-observed stars brighter than $Kp = 9$ in the *Kepler* field. This sample is biased towards red giants and hot stars, containing only a few FG dwarfs. We find no transiting planets, but detect *M* new eclipsing binaries, and solar-like oscillations in *N* red giants. We do not model hot stars or FG dwarfs in great detail, but provide some discussion and initial classification of interesting variability. For eclipsing binaries, we present the results of light-curve modelling to precisely determine their parameters. Finally, for the oscillating red giants, which constitute the bulk of the sample, we determine the asteroseismic parameters $\nu_{\rm max}$ and $\Delta\nu$, and therefore stellar masses and $\log g$ measurements; and we and obtain high-resolution spectroscopy with the Tillinghast Reflector Échelle Spectrograph (TRES), from whose spectra we derive stellar parameters and elemental abundances constrained by asteroseismic parameters. We discuss the potential for these as benchmark stars for other stellar surveys, in particular *Gaia*.

We have made all new data products and software discussed in this paper publicly available, and encourage interested readers to use these in their own research.

2 METHOD

In this Section we will discuss the methods used for characterizing our new benchmark stars. We have obtained smear light curves for our sample of red giant stars with the `keplersmear` pipeline as described in Section 2.2, performed asteroseismology on all of these to extract $\nu_{\rm max}$ and therefore $\log g$ as described in Section 2.3, and combined these with TRES spectra to obtain chemical abundances as described in Section 2.4.

2.1 Sample

We selected as our sample all stars on-silicon in *Kepler* with $Kp < 9$ which were unobserved for more than 8 quarters, including those stars which were entirely unobserved. A number of these lay just at the edge of a detector, with the result that in some cadences the centroid of the star did not lie on the chip; light curves from these targets were found to be of extremely low quality and all of these objects were discarded. After applying these criteria we obtained a list of 102 targets, which are listed in Table 1 in order of their *Kepler* magnitude Kp together with their spectral type from SIMBAD, *Gaia* DR2 source identifiers, apparent G magnitudes and distances from Bailer-Jones et al. (2018), the quarters for which the stars were observed, and whether spectroscopy is available as in Section 2.4 and Table 3. The *Kepler* satellite rotates between quarters, so that it cycles through four orientation 'seasons' each rotated from the last by 90°. Some stars did not land on silicon for all seasons: we have only one season of HD 179394; two for HD 187277, HD 226754, V554 Lyr, and BD+47 2891; and three for BD+43 3064. Aside from the restriction on stars falling on the edge

of a chip like this or otherwise, the addition of our sample to the conventionally-observed stars makes the *Kepler* survey magnitude-complete down to $Kp = 9$.

In Figure 1 we show these stars on a colour-magnitude diagram in *Gaia* $Bp - Rp$ and absolute G magnitudes using *Gaia* DR2 calibrated distances from Bailer-Jones et al. (2018), and situate these in context with the entire *Kepler* sample from the Bedell `gaia-kepler.fun` crossmatch. While *Gaia* parallaxes for very bright stars can be subject to systematic error, we have compared these to those found by *Hipparcos* (van Leeuwen 2007), and found close agreement for the brightest stars, with a scatter that increases with magnitude. From the HR diagram, we identify 64 of these objects as evolved systems, and the remaining 38 lie on the main sequence. One of the main sequence objects, BD+43 3068 is a G0 dwarf with a G magnitude of 8.267944 and a distance of 53.8 ± 0.1 pc, and it is therefore surprising that it was not included in the nominal *Kepler* survey as a Solar analogue: it is possible that it was previously misidentified as a giant. Regrettably, it is only possible to reconstruct a light curve with the 30 minute long cadence and therefore it is not possible to do asteroseismology on this bright, nearby solar-like star.

2.2 Photometry

In preparing light curves of the *Kepler* smear stars, we follow the methods described in Pope et al. (2016), with some improvements. We select using RA and Dec values from the *Kepler* Input Catalog (KIC) (Brown et al. 2011), and query MAST to find the corresponding mean pixel position for a given *Kepler* quarter. We measure the centroid of smear columns in the vicinity, and use these values to do raw aperture photometry. We find that the cosine-bell aperture used for raw photometry in Pope et al. (2016) can in some light curves introduce position-dependent systematics and jumps. We instead in this work apply a super-Gaussian aperture, $A \propto \exp \frac{-(x - x_0)^4}{w}$, where x_0 is the centroid and w a width in pixels. The very flat top of this function helps avoid significant variation with position, while still smoothly rolling off at the edges to avoid discontinuous artefacts. We calculate this on a grid of $10\times$ subsampled points in pixel space so that the sharply varying edge changes column weights smoothly as a function of centroid. We extract photometry using apertures with a range of widths $w \in \{1.5,\ 2,\ 3,\ 4,\ 5\}$ pixels.

From this raw photometry we subtract a background light curve, which corrects for time-varying global systematics. Whereas in Pope et al. (2016) we then subtract a background estimate chosen manually, for this larger set of light curves, we now choose the lowest 25% of pixels by median flux as being unlikely to be contaminated by stars, and take our background level to be the median of this at each time sample. To denoise this, we fit a Gaussian Process with a 30-day timescale squared exponential kernel using GEORGE (Ambikasaran et al. 2015), and our final background light curve is taken to be the posterior mean of this GP.

The dominant source of residual systematic errors in nominal *Kepler* time series is a common-mode variation primarily due to thermal changes on board the spacecraft, an issue which is traditionally dealt with by identifying and fitting a linear combination of systematic modes (Twicken et al. 2010; Stumpe et al. 2012; Smith et al. 2012; Petigura & Marcy 2012). We adopt the same approach here, using the *Kepler* Pre-search Data Conditioning (PDC) Cotrending Basis Vectors (CBVs) available from MAST, finding least-squares fits of either the first 4 or 8 CBVs to each light curve. We note that this can subtract astrophysical signals on long timescales, such that we use and recommend 4 CBV light curves for stars with variability on timescales longer than ∼ 5 days, but otherwise use the 8 CBV light curves. There is some room for improvement here by simultaneously modelling astrophysical and instrumental variations, but this is beyond the scope of this paper. In the following, we will use the light curves with the lowest 6.5 hr Combined Differential Photometric Precision (CDPP) (Christiansen et al. 2012) out of all apertures, as calculated with the κ2sc implementation (Aigrain et al. 2016). This is not necessarily the optimal choice for all red giants, especially those with oscillations on a 6.5 h timescale, but is a reasonable proxy nevertheless for white noise and leads to satisfactory results upon visual inspection of the present sample.

2.3 Asteroseismology

For all N red giants identified in this sample, we have attempted to extract the asteroseismic parameters $\nu_{\rm max}$ and $\langle\Delta\nu\rangle$ (Kjeldsen & Bedding 1995; Chaplin & Miglio 2013). These constrain fundamental stellar parameters independently from spectroscopic or interferometric measurements:

$$\nu_{\rm max} \propto \frac{g}{g_\odot} \cdot \frac{T_{\rm eff}}{T_{\rm eff\,\odot}} \frac{1}{2} \tag{1}$$

and

$$\langle\Delta\nu\rangle \propto \sqrt{\langle\rho\rangle} = \sqrt{\frac{M}{\rm M_\odot}(\frac{R}{\rm R_\odot})^{-3}} \tag{2}$$

We follow the method of Davies & Miglio (2016), obtaining a Lomb-Scargle periodogram of the smoothed time series according to the method of García et al. (2011). We then conduct a Markov Chain Monte Carlo fit to this, applying the combined granulation and oscillation model of Kallinger et al. (2014), consisting of two Harvey profiles for the granulation (Harvey 1985), a Gaussian envelope for the stellar oscillations, and a white noise background for instrumental noise. We find that the marginal posterior distribution for the Gaussian envelope is well-approximated by a single Gaussian, and take its median and standard deviation to be our estimates for $\nu_{\rm max}$ and its uncertainty.

To estimate $\Delta\nu$, we divide the power spectrum through by the granulation and noise models to obtain a signal-to-noise spectrum, and fit a sum of Lorentzians separated by mean large ($\Delta\nu$) and small ($\delta\nu$) separations to the part of this spectrum in the vicinity of $\nu_{\rm max}$. In practice, for this dataset, $\delta\nu$ is poorly constrained, but mean $\langle\Delta\nu\rangle$ is typically well-constrained and its posterior marginal distribution is well-represented by a single Gaussian as with $\nu_{\rm max}$.

We obtain good estimates of these asteroseismic parameters for 35 targets, presented in Table 2. In many of the remainder of cases, we find that the very-low-frequency ($\lesssim 2\mu$Hz) oscillations are affected by filter artefacts from detrending, and we are not able to obtain good estimates for these stars.

Once $\nu_{\rm max}$ has been estimated, we use the asteroseismic scaling relation for $\nu_{\rm max}$ (Equation 1; Kjeldsen & Bedding 1995) to estimate $\log g$ in order to inform extraction of chemical abundances from spectra. Using the initial spectroscopic estimate of $T_{\rm eff}$, which is not significantly informed by $\nu_{\rm max}$, we propagate uncertainties in $\nu_{\rm max}$ with Monte Carlo sampling.

For eight stars, we find that the asteroseismic fit is unsatisfactory: for BD+39 388 we cannot detect the expected oscillations;

Table 1. The full set of underobserved and unobserved stars for which new light curves have been produced in this smear catalogue. Calibrated *Gaia* distances are from (Bailer-Jones et al. 2018). Some objects, such as HD 185351, were observed in long cadence in some quarters and short cadence in others, and this is noted accordingly. The eclipsing binary V2083 Cyg was detected by *Gaia*, but a parallax could not be obtained in DR2, possibly due to binary motion.

Object	Spectral Type (SIMBAD)	Kp (mag)	G (mag)	*Gaia* Distance (pc)	*Gaia* ID	Observed	Spectroscopy
HD 185351	G8.5IIIbFe-0.5	5.034	4.881522	$41.2^{+0.1}_{-0.1}$	2078403295235690112	LC:Q1-3 SC:Q16	TRES
HD 186155	F5II-III	5.055	4.923168	$50.6^{+0.4}_{-0.4}$	2079990268465009024	LC:Q1	–
HD 175740	G8III	5.212	5.152375	$81.5^{+0.6}_{-0.6}$	2104485016711846656	unobserved	TRES
HD 184875	A2V	5.403	5.2788925	$172.6^{+3.3}_{-3.2}$	2077737571001053312	unobserved	–
14 Cyg	B9III	5.49	5.3699827	$194.3^{+7.0}_{-6.6}$	2077959092540451456	unobserved	–
HD 189178	B5V	5.552	5.41016	$347.3^{+13.0}_{-12.1}$	2073537612700605696	unobserved	–
HD 187372	M1III	5.672	5.3131795	$306.4^{+10.3}_{-9.6}$	2086614688589352320	unobserved	–
HD 182694	G7IIIa	5.722	5.598205	$133.1^{+0.7}_{-0.7}$	2126062687590513408	LC:Q2	TRES
V380 Cyg	B1.1III+B2.5/3V:	5.771	5.6319346	$1044.7^{+116.6}_{-95.6}$	2073743839843579776	LC:Q11 SC:Q7 9 10 12-17	–
HD 186121	M3III	5.773	5.1762185	$475.2^{+35.1}_{-30.7}$	2078059800932315008	unobserved	–
HD 189684	A5III	5.982	5.8811946	$125.2^{+6.2}_{-5.7}$	2085224321778525696	unobserved	–
HD 188252	B2III	6.007	5.864375	$1000.6^{+82.6}_{-71.1}$	2086465429887466368	LC:Q13	–
HD 181597	K1III	6.04	5.985134	$135.8^{+0.3}_{-0.3}$	2132637359106746880	unobserved	TRES
HD 185286	K5	6.151	6.055302	$263.5^{+3.9}_{-3.8}$	2078199335828818432	unobserved	TRES
HD 188875	K2	6.164	6.091042	$683.8^{+12.4}_{-11.9}$	2073542697941496320	unobserved	TRES
HD 175466	K2	6.165	5.9186597	$397.8^{+6.8}_{-6.6}$	2104983267278926336	unobserved	–
V547 Lyr	M4-IIIa	6.199	5.227579	$288.9^{+13.1}_{-12.0}$	2103815448491466496	unobserved	–
HD 175884	K0	6.21	6.144104	$238.9^{+1.5}_{-1.4}$	2104876786449045504	unobserved	TRES
HD 181069	K1III	6.279	6.264174	$144.2^{+0.6}_{-0.6}$	2101000011531700480	LC:Q1 10 13 14 17	TRES
HD 179959	K0	6.28	6.2575774	$499.2^{+7.2}_{-7.0}$	2130848621187317632	unobserved	TRES
V543 Lyr	B3V	6.299	6.159548	$345.1^{+5.6}_{-5.4}$	2103449001881575680	unobserved	–
HD 182354	K0	6.32	6.2906675	$228.9^{+1.7}_{-1.7}$	2051085757046109184	unobserved	–
HD 175132	B9IIIpSi	6.362	6.242306	$333.3^{+5.9}_{-5.7}$	2104376989694932608	unobserved	–
V819 Cyg	B0.5IIIn	6.381	6.243083	$1114.0^{+70.9}_{-63.0}$	2086460069767734656	LC:Q14 16 17	–
HD 183362	B3Ve	6.394	6.2077436	$571.1^{+18.2}_{-17.2}$	2051905889641367296	unobserved	–
HD 187217	K0	6.399	6.3447323	$243.2^{+1.8}_{-1.8}$	2135282371768942464	LC:Q14-17	TRES
HD 183124	G8II	6.441	6.3954253	$160.7^{+0.8}_{-0.8}$	2126627291112264192	LC:Q2 4 6 8 10 12 14 16	TRES
HD 190149	M0II-III	6.488	6.1712503	$409.4^{+3.8}_{-3.7}$	2076072811625087104	unobserved	–
HD 181022	K5	6.496	6.2475405	$317.7^{+2.7}_{-2.7}$	2099498216086406784	unobserved	TRES
HD 176582	B5V	6.51	6.383207	$298.6^{+3.9}_{-3.8}$	2100218568000743680	LC:Q12-13	–
HD 174177	A2IV	6.575	6.4831395	$223.9^{+1.7}_{-1.6}$	2119115290229197568	unobserved	–
HD 180682	K0	6.617	6.5322237	$295.8^{+2.5}_{-2.5}$	2101317839111655424	LC:Q0 3 7	TRES
HD 181878	G5	6.698	6.5869	$259.5^{+1.8}_{-1.8}$	2101141023898417920	LC:Q14-17	–
HD 174020	K5	6.753	6.6002703	$433.1^{+4.2}_{-4.1}$	2117257184298759424	LC:Q2 6 10 14	TRES
HD 184787	A0V	6.757	6.658364	$139.6^{+1.1}_{-1.1}$	2077629170330851072	unobserved	–
HD 178090	K5	6.758	6.5490265	$583.0^{+8.5}_{-8.3}$	2105455919840116096	LC:Q1 3 10	–
HD 181681	K4III	6.864	6.6958766	$585.0^{+9.1}_{-8.9}$	2101161742821561728	unobserved	–
HD 175841	A2	6.885	6.797499	$241.0^{+2.1}_{-2.1}$	2103508478587989504	LC:Q11-12 14-16 SC:Q3	–
V2083 Cyg	A3	6.902	6.81	–	2128480311802353536	unobserved	–
HD 189013	A2	6.922	6.8403153	$188.8^{+6.4}_{-6.0}$	2085660209419178496	SC:Q3 gDor	–
HD 183203	K5	6.928	6.5295672	$476.9^{+5.9}_{-5.8}$	2136136967178617216	unobserved	–
HD 176626	A2V	6.933	6.84066	$224.8^{+1.8}_{-1.7}$	2105841848421613568	unobserved	–
HD 181521	A0	6.939	6.8521805	$217.8^{+3.4}_{-3.3}$	2101352439367659904	unobserved	–
HD 185397	A5	6.953	6.8550224	$180.0^{+1.0}_{-1.0}$	2052171078106937728	unobserved	–
HD 186255	A3	6.966	6.8618903	$254.5^{+4.1}_{-4.0}$	2076294397581835136	unobserved	–
HD 174829	K0	6.967	6.9280105	$355.0^{+3.5}_{-3.4}$	2105159257858400640	unobserved	TRES
V398 Lyr	M3	7.024	5.4027195	$494.7^{+34.9}_{-30.6}$	2100382189073830528	unobserved	–
HD 181596	K5III	7.05	6.862713	$591.1^{+8.1}_{-7.8}$	2133045380999412608	unobserved	–
HD 179395	B9	7.168	7.0700407	$233.9^{+1.7}_{-1.7}$	2102450954560072320	unobserved	–
V2079 Cyg	B8V	7.174	7.034088	$321.5^{+3.7}_{-3.6}$	2126627978307068672	unobserved	–
HD 181328	M1	7.182	6.6139154	$353.9^{+3.3}_{-3.3}$	2133256109274840448	unobserved	–
HD 184483	M5	7.246	6.7187505	$492.9^{+5.5}_{-5.4}$	2126262042793757696	unobserved	–

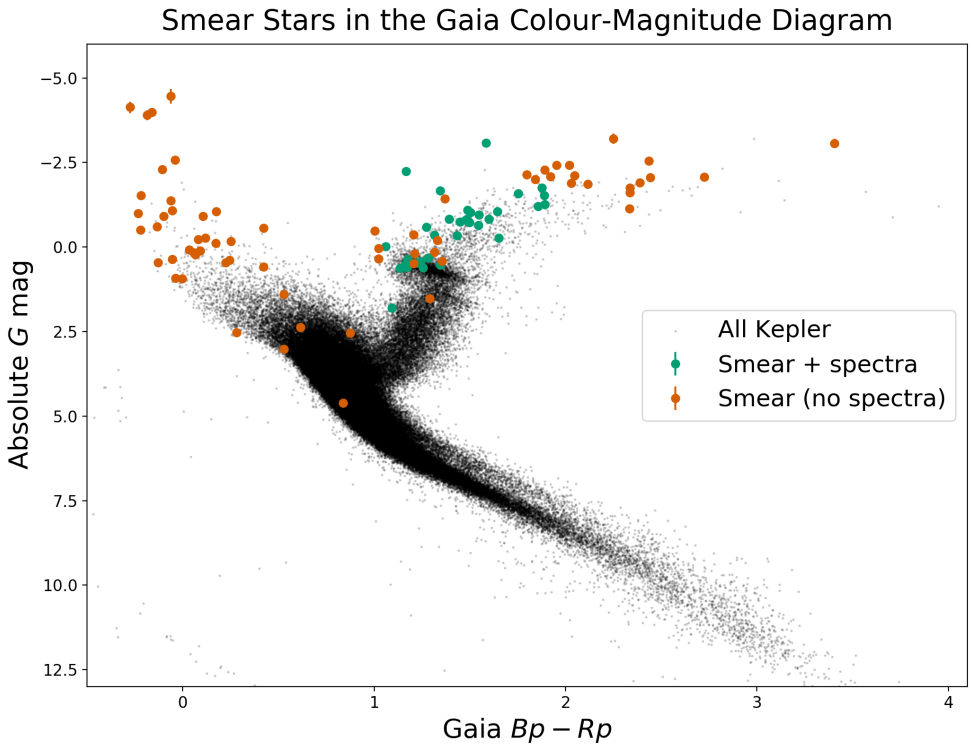

Figure 1. *Gaia* colour-magnitude diagram of the Smear Campaign stars (orange and teal) situated in sample of *Kepler* stars with *Gaia* parallax SNR > 25 (black), using the Bedell `gaia-kepler.fun` crossmatch and *Gaia* DR2 calibrated distances from Bailer-Jones et al. (2018). The smear sample includes giants and hot main-sequence stars. Those giants for which TRES spectroscopy have been obtained are highlighted in teal. An interactive version of this diagram is available as supplementary material from the journal or at `benjaminpope.github.io/data/cmd_smear.html`.

BD+43 3064 there are significant peaks but these are not consistent with the pattern expected from a red giant; for HD 179959 and HD 187217 we suspect contamination with the oscillations of a second giant, which is hard to remove from smear light curves; while for HD 188629, HD 188639 and HD 188875 we can extract a $\nu_{\rm max}$ but not a robust $\Delta\nu$. One star in our sample, the retired A star HD 185351, has a mode envelope that is not well fit by our model. The smear light curve for this star has already been published by Hjørringgaard et al. (2017), who showed with detailed asteroseismic modelling that it had a zero-age main sequence mass of $\sim 1.60 M_\odot$ and used it to calibrate the convective overshoot parameter for low-luminosity red giants. The bulk asteroseismic modelling presented here should therefore be considered to be superseded by the more detailed model of Hjørringgaard et al. (2017).

2.4 Spectroscopy

For the whole red giant sample, we have obtained high-resolution spectroscopy with TRES in order to constrain stellar parameters and elemental abundances. Operating with spectral resolving power R = 44000, we obtain signal-to-noise ratios of tens to hundreds per resolution element. We note that this resolution and SNR are sufficient for an exploratory study, but for more detailed analysis it will be desirable to use APOGEE or similar instruments at higher resolution and SNR. From this observing run we have 35 unique targets with seismic $\log g$ and spectra, one more star than the *Gaia*-ESO benchmark set and a significant addition to the ensemble of bright red giants with asteroseismic parameter determinations. These are unfortunately not the same 35 unique targets as for the asteroseismic analysis presented above in Section 2.3: due to observing constraints, we were unable to obtain spectra for BD+42 315, BD+48 290, HD 176209, HD 182354, HD 189636, or HD 189750.

To derive stellar parameters from our TRES spectra, we initially run the Stellar Parameter Classification (SPC: Buchhave et al. 2012) code to determine $T_{\rm eff}$ and $\log g$, using the SPC $T_{\rm eff}$ to inform the asteroseismic estimation of $\log g$ from $\nu_{\rm max}$. For deriving abundances, $T_{\rm eff}$ is fixed from the results of an initial SPC fit, while $\log g$ is fixed to the seismic values. The other stellar atmospheric parameters including the microturbulent velocity ($\nu_{\rm mic}$), and broadening (convolution by $V_{\rm mac}$, $\nu_{\sin i}$ and the instrumental line profile) as well as [Fe/H] and chemical abundances for 20 chemical species are derived using the Brussels Automatic Code for Characterizing High accUracy Spectra (BACCHUS: Masseron et al. 2016), and the results from this calculation are displayed in Table 3. BACCHUS uses an interpolation scheme through a grid of MARCS model atmospheres (Gustafsson et al. 2008) in combination with TURBOSPECTRUM (Alvarez & Plez 1998; Plez 2012). For the calculation of synthetic spectra, atomic line information has been taken from the fifth version of the Gaia-ESO linelist (Heiter et al., in preparation). Additionally we used the molecular species for CH (Masseron et al. 2014), CN, NH, OH, MgH C_2 (T. Masseron, private communication). The SiH molecular information is adopted

Table 1 – *continued* The full set of underobserved and unobserved stars for which new light curves have been produced in this smear catalogue. Calibrated *Gaia* distances are from (Bailer-Jones et al. 2018).

Object	Spectral Type (SIMBAD)	Kp (mag)	G (mag)	*Gaia* Distance (pc)	*Gaia* ID	Observed	Spectroscopy
HD 184788	B9	7.249	7.1427946	$226.5^{+2.4}_{-2.3}$	2077414353248711168	unobserved	–
HD 184147	B9IV	7.251	7.1445045	$175.5^{+2.6}_{-2.5}$	2128261058011465088	unobserved	–
BD+42 3367	M0	7.271	6.991751	$762.0^{+15.8}_{-15.2}$	2125866188548442240	unobserved	–
HD 177697	K5	7.3	6.7638826	$472.0^{+5.4}_{-5.3}$	2100727362705844608	unobserved	–
HD 182692	K0	7.31	7.247128	$226.6^{+1.3}_{-1.3}$	2129216847153832576	unobserved	TRES
HD 178797	K0	7.312	7.2491374	$406.1^{+4.8}_{-4.7}$	2130641367544915584	unobserved	TRES
HD 184215	B8	7.321	7.188762	$361.2^{+6.4}_{-6.1}$	2128924750717810560	unobserved	–
HD 188537	K0	7.382	7.3244863	$629.9^{+11.4}_{-11.0}$	2079411684837733376	unobserved	TRES
V546 Lyr	M3III	7.385	6.784268	$587.8^{+13.1}_{-12.6}$	2104055760501638016	unobserved	–
HD 176209	A0	7.437	7.3647585	$282.2^{+2.7}_{-2.7}$	2107207888539182464	unobserved	–
HD 174676	–	7.481	7.4398384	$993.3^{+26.7}_{-25.4}$	2105176094130309120	unobserved	–
HD 186727	M0	7.499	6.9165545	$581.7^{+9.2}_{-8.9}$	2135406788381171328	unobserved	–
HD 181778	K0	7.545	7.513725	$374.5^{+3.4}_{-3.4}$	2102822898727875968	unobserved	TRES
HD 179394	B8	7.575	7.475068	$476.2^{+12.2}_{-11.6}$	2102561730358498048	unobserved	–
HD 187277	A0	7.579	7.4642863	$96.9^{+0.4}_{-0.4}$	2077186823061026688	unobserved	–
HD 186994	B0III	7.585	7.4506955	$1866.1^{+138.1}_{-120.6}$	2079735628451463296	unobserved	–
HD 183383	B9	7.64	7.5365596	$357.1^{+5.5}_{-5.3}$	2101750806176118272	unobserved	–
HD 180475	K2	7.664	7.5950294	$546.1^{+8.0}_{-7.8}$	2132690273103943296	unobserved	TRES
BD+42 3393	K5	7.664	7.4138913	$929.0^{+25.9}_{-24.5}$	2077747333469959168	unobserved	–
HD 185117	K5	7.696	7.472238	$817.7^{+14.8}_{-14.3}$	2127965946519825664	unobserved	–
HD 176894	F0	7.7	7.6103888	$82.8^{+0.2}_{-0.2}$	2104067683330612992	unobserved	–
HD 188629	K5	7.743	7.5462255	$651.0^{+12.0}_{-11.6}$	2079112926916521472	unobserved	TRES
HD 177781	G5	7.744	7.700899	$296.2^{+2.6}_{-2.5}$	2099949359449611648	unobserved	–
HD 182737	A0	7.82	7.757723	$460.3^{+6.7}_{-6.5}$	2051765044774262656	unobserved	–
HD 226754	K2	7.829	7.702354	$391.8^{+6.1}_{-5.9}$	2075352803312372224	unobserved	TRES
HD 178910	K2	7.864	7.8481197	$291.3^{+2.4}_{-2.4}$	2131298291383139712	unobserved	TRES
HD 181097	K0	7.92	7.8478937	$434.3^{+6.2}_{-6.0}$	2101003000830222336	unobserved	TRES
HD 180658	K0	7.932	7.870914	$282.2^{+2.3}_{-2.3}$	2102227135227203968	unobserved	TRES
HD 182531	K5	7.955	7.8590217	$599.3^{+9.2}_{-8.9}$	2129553606948677120	unobserved	TRES
BD+48 2955	K2	7.961	7.8992686	$589.4^{+11.6}_{-11.1}$	2086732572553136896	unobserved	TRES
HD 180312	K0II	7.97	7.8340764	$290.5^{+2.4}_{-2.4}$	2099729349754501888	unobserved	TRES
HD 184565	K0	7.972	7.9430523	$380.9^{+4.3}_{-4.2}$	2077577115326313472	unobserved	–
HD 181880	K	7.982	7.940268	$541.2^{+10.1}_{-9.7}$	2052869611580098688	unobserved	TRES
HD 179396	K2	8.001	7.9701843	$321.2^{+2.7}_{-2.6}$	2099631394432060416	unobserved	TRES
HD 185524	K2	8.022	7.9525204	$753.4^{+15.9}_{-15.2}$	2079919315611727616	unobserved	–
HD 189636A	–	8.025	8.118049	$384.7^{+6.0}_{-5.8}$	2085638116106993408	unobserved	–
HD 189750	K0	8.052	8.060998	$327.0^{+3.0}_{-2.9}$	2076143588378412416	unobserved	–
HD 189636B	–	8.107	8.023957	$376.4^{+4.9}_{-4.7}$	2085638116106991872	unobserved	–
BD+36 3564	K5	8.128	8.040623	$547.1^{+11.6}_{-11.1}$	2051728490311183744	unobserved	TRES
BD+39 3577	G5	8.131	8.089526	$311.7^{+2.7}_{-2.7}$	2103507894472422656	unobserved	TRES
V554 Lyr	–	8.179	8.092074	$335.7^{+4.6}_{-4.5}$	2101290316961062400	unobserved	–
BD+47 2825	K0	8.251	8.236473	$485.8^{+7.3}_{-7.1}$	2129162799284981760	unobserved	–
BD+39 3882	F5	8.259	8.158849	$143.3^{+0.7}_{-0.7}$	2076372669064227200	unobserved	–
BD+43 3064	K5	8.284	8.20331	$641.0^{+20.3}_{-19.1}$	2117284053614333312	unobserved	TRES
BD+43 3068	G0	8.308	8.267944	$53.8^{+0.1}_{-0.1}$	2117267079903573504	unobserved	–
BD+43 3213	K5	8.311	8.13925	$948.8^{+25.8}_{-24.5}$	2102821524341578496	unobserved	TRES
BD+42 3150	K0	8.35	8.31532	$546.0^{+32.5}_{-29.1}$	2116742544137540608	unobserved	–
BD+43 3171	M0	8.373	8.178079	$751.5^{+17.2}_{-16.5}$	2105998150870718080	unobserved	TRES
BD+48 2904	K0	8.487	8.439092	$400.9^{+5.4}_{-5.3}$	2129676443013218304	unobserved	–
BD+47 2891	K0	8.68	8.6254015	$262.8^{+1.7}_{-1.6}$	2128576003674178688	unobserved	–

from the Kurucz linelists and the information for TiO, ZrO, FeH, CaH from B. Plez (private communication).

Individual elemental abundances are derived by first fixing the stellar atmospheric parameters to those determined above. Spectra are then synthesized in regions centered around an absorption feature of the element we want to derive. The spectra generated will have different [X/Fe] values. A χ^2 minimization procedure is then done to derive the best fitting abundance for each line. The reported abundances are the median [X/Fe] value of the various line regions for a given element. To achieve the most precise abundances we have derived them using both with and without a line-by-line differential approach with respect to Arcturus (α Boötis) using the method described by Jofré et al. (2015) and the Arcturus abundances from (Hawkins et al. 2016c). The results of these absolute

Table 2. Bulk asteroseismic parameters $\Delta\nu$, $\nu_{\rm max}$, and ϵ for the red giant sample as discussed in Section 2.3.

Object	$\Delta\nu$ (μHz)	$\nu_{\rm max}$ (μHz)	ϵ
BD+36 3564	0.95 ± 0.03	5.08 ± 0.10	0.83 ± 0.20
BD+39 3577	1.68 ± 0.01	13.27 ± 0.32	0.74 ± 0.06
BD+42 3150	4.22 ± 0.03	38.32 ± 0.96	0.70 ± 0.07
BD+43 3171	0.42 ± 0.05	1.98 ± 0.05	0.80 ± 0.17
BD+43 3213	0.49 ± 0.01	2.56 ± 0.06	1.01 ± 0.07
BD+48 2904	2.85 ± 0.01	23.13 ± 0.72	0.86 ± 0.08
BD+48 2955	0.90 ± 0.01	5.44 ± 0.08	0.81 ± 0.05
HD 174020	0.56 ± 0.02	2.48 ± 0.10	0.89 ± 0.08
HD 174829	1.28 ± 0.01	7.95 ± 0.16	0.78 ± 0.06
HD 175740	5.93 ± 0.01	64.33 ± 0.78	1.00 ± 0.02
HD 175884	1.12 ± 0.01	7.07 ± 0.11	0.96 ± 0.08
HD 176209	4.22 ± 0.08	36.08 ± 0.77	0.87 ± 0.06
HD 178797	1.03 ± 0.02	6.34 ± 0.09	0.74 ± 0.29
HD 178910	3.64 ± 0.02	32.06 ± 0.31	0.83 ± 0.05
HD 179396	3.76 ± 0.02	31.02 ± 0.44	0.92 ± 0.03
HD 180312	4.17 ± 0.02	33.84 ± 0.28	0.96 ± 0.04
HD 180475	0.82 ± 0.00	4.34 ± 0.10	0.68 ± 0.03
HD 180658	4.00 ± 0.02	33.76 ± 0.50	0.90 ± 0.05
HD 180682	0.77 ± 0.05	3.68 ± 0.08	1.07 ± 0.15
HD 181022	0.38 ± 0.01	1.58 ± 0.03	0.70 ± 0.10
HD 181069	4.43 ± 0.01	41.46 ± 0.32	0.90 ± 0.02
HD 181097	1.61 ± 0.02	11.16 ± 0.14	0.72 ± 0.36
HD 181597	3.11 ± 0.01	25.84 ± 0.25	0.97 ± 0.02
HD 181778	2.56 ± 0.02	22.86 ± 0.29	0.72 ± 0.06
HD 181880	1.04 ± 0.01	6.54 ± 0.10	0.76 ± 0.05
HD 182354	2.66 ± 0.01	24.73 ± 0.37	0.74 ± 0.04
HD 182531	1.03 ± 0.00	6.47 ± 0.09	0.86 ± 0.03
HD 182692	4.66 ± 0.01	44.38 ± 0.47	0.87 ± 0.02
HD 182694	5.71 ± 0.01	69.78 ± 1.02	0.94 ± 0.25
HD 183124	4.39 ± 0.01	39.59 ± 0.29	0.95 ± 0.03
HD 185286	0.72 ± 0.01	4.23 ± 0.10	0.73 ± 0.08
HD 188537	1.55 ± 0.01	13.40 ± 0.34	0.72 ± 0.07
HD 189636	2.91 ± 0.01	25.97 ± 0.74	0.97 ± 0.04
HD 189750	4.16 ± 0.04	36.14 ± 0.58	0.94 ± 0.08
HD 226754	1.19 ± 0.01	7.41 ± 0.19	0.74 ± 0.08

abundance calculations **without the line-by-line differential analysis implemented?**, are presented in Tables 4, 5 and 6. Because for most elements Arcturus differential abundances are not available, these are provided as supplementary online-only material. No abundances for oxygen could be reliably derived for any of the stars in our spectroscopic sample by either method.

3 RESULTS

3.1 Red Giants

3.1.1 Chemical Composition

place [X/Fe] vs [Fe/H] diagrams here and discuss which Galactic populations these stars come from. May also want to discuss how these span the typical Galactic populations and can act as benchmark stars for APOGEE or other large surveys

3.1.2 Red Clump Stars

Red clump stars, which burn helium in their cores, differ significantly in their core structure from stars on the hydrogen shell burning red giant sequence. They can therefore be distinguished from hydrogen-shell burning giants asteroseismologically, due to their much higher g-mode period spacings (Bedding et al. 2011). The moniker 'red clump' arises from the fact that such stars can have a very narrow range of luminosities, so that they appear as a clump in the HR diagram (Girardi 2016). This property makes them useful standard candles to which distances can be accurately computed from photometry. Red clump stars have been used to calibrate the *Gaia* survey's parallaxes at long distances (Davies et al. 2017; Hawkins et al. 2017; Ruiz-Dern et al. 2018). *Gaia* DR2 parallaxes have a zero-point offset of ~ 0.03 mas (Lindegren et al. 2018), and in particular hierarchical models of the ensemble of *Gaia* clump stars can be used to accurately estimate this and thereby improve the accuracy of *Gaia* distances greater than a few kpc (Hawkins et al., in prep.).

From visual inspection of the power spectra, HD 181069, HD 183124, HD 182354, HD 182692, and HD 180658 are seen to be red clump stars. A power spectrum of the best example of these, HD 183124, together with an échelle diagram used to estimate its g-mode period spacing, is shown in Figure 2. While precise characterization of these stars to the necessary degree is beyond the scope of this paper, they are ideal candidates for anchoring models of the mass and metallicity dependence of red clump properties for calibrating *Gaia* and other distance measures.

3.2 Main Sequence Pulsators

Two stars in the sample show the 'hump-and-spike' morphology in their power spectra (a broad 'hump' of low-amplitude oscillations dominated by one high amplitude coherent oscillation): HD 186155 (HR 7495), and HD 183362 (HR 7403), respectively the third brightest and 37$^{\rm th}$-brightest stars on silicon and the brightest two stars that show this effect. Saio et al. (2018) have recently claimed the hump-and-spike power spectra as evidence for Rossby modes. The F5 star HD 186155, identified by SIMBAD as having a giant spectral type of F5II-III, is shown by its *Gaia* distance to in fact lie on the main sequence. The other example is the B3e star HD 183362 at $G = -2.576$. A detailed study of these stars will be presented by Antoci et al., in prep.

Another star with a hump-and-spike spectrum is Boyajian's Star, which shows deep enigmatic dips in brightness (Boyajian et al. 2016), and has faded both throughout the *Kepler* mission (Montet & Simon 2016) and in relation to Harvard photographic plates from 1890 onwards (Schaefer 2016). The dimming, which is chromatic in the manner expected of heterogeneous clouds of circumstellar dust in the line of sight (Davenport et al. 2018; Bodman et al. 2018), has been ascribed to various causes (reviewed in Wright 2018), most notably a cloud of exocomets surrounding the star (e.g. Wyatt et al. 2018). It is unclear whether the explanation of the hump-and-spike phenomenon will shed light on the strange behaviour of Boyajian's Star, but it may be relevant.

Ashley/Dan/Vichi?

3.3 Eclipsing Binaries

4 OPEN SCIENCE

We believe in open science, and have therefore made all substantive products of this research available to the interested reader. All code used to produce smear light curves is available under a GPL v3 license at `github.com/benjaminpope/keplersmear`. All smear light curves, both including the red giant sample studied in detail in

Table 3. Fundamental stellar parameters for the red giant sample as determined jointly by asteroseismology (asteroseismic log g; Section 2.3) and spectroscopy (RV, $T_{\rm eff}$, log g, [M/H], $V \sin i$, and SNR; Section 2.4.)

Object	RV (km/s)	$T_{\rm eff}$ (K)	log g	[M/H]	$V \sin i$ (km/s)	SNR
BD+36 3564	−77.84 ± 0.05	4301 ± 50	2.06 ± 0.10	−0.34 ± 0.08	5.14 ± 0.50	71.8
BD+39 3577	−14.81 ± 0.07	5079 ± 50	3.00 ± 0.10	−0.11 ± 0.08	3.98 ± 0.50	92.8
BD+43 3064	−13.65 ± 0.06	4266 ± 50	2.03 ± 0.10	−0.21 ± 0.08	5.17 ± 0.50	69.2
BD+43 3171	−16.32 ± 0.11	4072 ± 50	2.02 ± 0.10	−0.17 ± 0.08	5.68 ± 0.50	68.6
BD+43 3213	−14.16 ± 0.16	4131 ± 50	2.07 ± 0.10	0.07 ± 0.08	6.24 ± 0.50	57.3
BD+48 2955	1.66 ± 0.04	4344 ± 50	2.11 ± 0.10	−0.32 ± 0.08	4.78 ± 0.50	31.7
HD 174020	−14.84 ± 0.08	4162 ± 50	1.97 ± 0.10	−0.10 ± 0.08	5.81 ± 0.50	120.1
HD 174829	10.15 ± 0.03	4482 ± 50	2.06 ± 0.10	−0.40 ± 0.08	4.41 ± 0.50	112.2
HD 175740	−8.82 ± 0.05	4973 ± 50	2.97 ± 0.10	−0.05 ± 0.08	3.66 ± 0.50	264.0
HD 175884	−34.39 ± 0.07	4466 ± 50	2.22 ± 0.10	−0.27 ± 0.08	4.46 ± 0.50	144.4
HD 178797	6.35 ± 0.05	4406 ± 50	2.21 ± 0.10	−0.37 ± 0.08	4.18 ± 0.50	77.1
HD 178910	−14.28 ± 0.05	4589 ± 50	2.46 ± 0.10	0.14 ± 0.08	4.26 ± 0.50	76.9
HD 179396	24.80 ± 0.04	4781 ± 50	2.51 ± 0.10	−0.21 ± 0.08	3.99 ± 0.50	82.7
HD 179959	−38.52 ± 0.09	4965 ± 50	2.19 ± 0.10	−0.23 ± 0.08	7.81 ± 0.50	129.3
HD 180312	−21.94 ± 0.05	4916 ± 50	2.55 ± 0.10	−0.44 ± 0.08	4.05 ± 0.50	73.5
HD 180475	−45.90 ± 0.08	4398 ± 50	2.15 ± 0.10	−0.44 ± 0.08	4.39 ± 0.50	58.4
HD 180658	2.97 ± 0.06	4802 ± 50	2.57 ± 0.10	−0.12 ± 0.08	3.81 ± 0.50	72.3
HD 180682	30.99 ± 0.07	4410 ± 50	2.14 ± 0.10	−0.51 ± 0.08	4.88 ± 0.50	80.1
HD 181022	−80.39 ± 0.16	4045 ± 50	2.06 ± 0.10	−0.28 ± 0.08	5.75 ± 0.50	108.8
HD 181069	9.99 ± 0.05	4842 ± 50	2.70 ± 0.10	−0.05 ± 0.08	3.53 ± 0.50	90.0
HD 181097	−5.60 ± 0.08	4520 ± 50	2.31 ± 0.10	−0.28 ± 0.08	4.08 ± 0.50	69.7
HD 181597	−13.06 ± 0.04	4751 ± 50	2.67 ± 0.10	−0.23 ± 0.08	2.23 ± 0.50	161.8
HD 181778	−22.04 ± 0.06	4664 ± 50	2.34 ± 0.10	−0.19 ± 0.08	4.23 ± 0.50	87.6
HD 181880	0.56 ± 0.08	4405 ± 50	2.23 ± 0.10	−0.30 ± 0.08	4.44 ± 0.50	71.2
HD 182531	−7.34 ± 0.05	4413 ± 50	2.24 ± 0.10	−0.24 ± 0.08	4.39 ± 0.50	71.4
HD 182692	−8.01 ± 0.05	4965 ± 50	3.06 ± 0.10	0.09 ± 0.08	3.40 ± 0.50	72.8
HD 182694	−0.87 ± 0.06	5178 ± 50	2.98 ± 0.10	−0.12 ± 0.08	5.12 ± 0.50	187.2
HD 183124	14.96 ± 0.01	4911 ± 50	2.85 ± 0.10	−0.15 ± 0.08	5.19 ± 0.50	114.3
HD 185286	−13.70 ± 0.08	4301 ± 50	2.08 ± 0.10	−0.14 ± 0.08	5.16 ± 0.50	135.6
HD 185351	−5.18 ± 0.04	5244 ± 50	3.66 ± 0.10	0.03 ± 0.08	2.02 ± 0.50	202.3
HD 187217	1.64 ± 0.05	4718 ± 50	2.41 ± 0.10	−0.17 ± 0.08	8.25 ± 0.50	59.9
HD 188537	−18.03 ± 0.15	4961 ± 50	2.41 ± 0.10	−0.08 ± 0.08	10.68 ± 0.50	67.0
HD 188629	10.97 ± 0.08	4227 ± 50	2.01 ± 0.10	−0.10 ± 0.08	5.53 ± 0.50	51.3
HD 188875	−13.71 ± 0.08	4473 ± 50	1.95 ± 0.10	−0.17 ± 0.08	7.07 ± 0.50	143.2
HD 226754	18.66 ± 0.10	4370 ± 50	2.36 ± 0.10	0.08 ± 0.08	4.78 ± 0.50	62.5

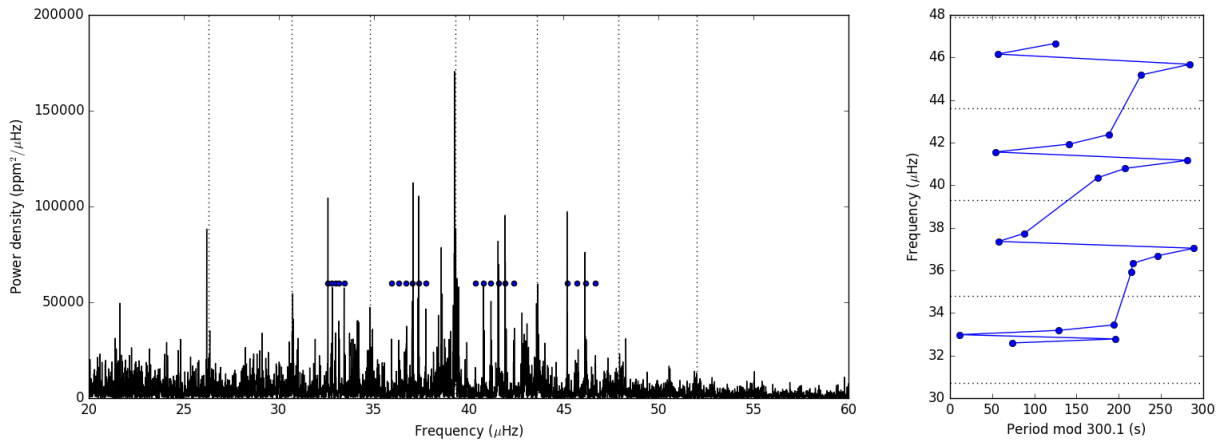

Figure 2. Power spectrum (left) and échelle diagram (right) of the solar-like oscillations of the red clump star HD 183124. The modes in the power spectrum used for the échelle diagram are highlighted with blue dots. In the échelle diagram we see the characteristic pattern of 'bumped' modes from avoided crossings between the comb of p-modes and g-mode oscillations with a period spacing of $\Delta\Pi$ = 300.1 s.

Table 4. Chemical abundances relative to iron for stars in the red giant sample as determined by BACCHUS, without differential line-by-line comparison to Arcturus, as described in Section 2.4, for the elements Ca, Mg, Si, Ti, Al, Ba, and Na. Dashes indicate elements for which abundances could not be reliably computed.The catalogue of abundances for more elements continues in Tables 5 and 6.

Object	[Ca/Fe]	[Mg/Fe]	[Si/Fe]	[Ti/Fe]	[Al/Fe]	[Ba/Fe]	[Na/Fe]
BD+36 3564	0.21 ± 0.02	0.33 ± 0.03	0.10 ± 0.03	0.34 ± 0.04	0.40 ± 0.01	–	0.26 ± 0.08
BD+39 3577	0.13 ± 0.02	0.22 ± 0.04	−0.11 ± 0.02	0.08 ± 0.04	0.21 ± 0.01	0.35 ± 0.10	0.42 ± 0.00
BD+43 3064	0.19 ± 0.04	0.21 ± 0.03	−0.01 ± 0.03	0.28 ± 0.04	0.36 ± 0.01	–	0.48 ± 0.06
BD+43 3171	0.29 ± 0.03	0.26 ± 0.06	−0.00 ± 0.07	0.21 ± 0.06	0.42 ± 0.01	0.33 ± 0.18	0.18 ± 0.25
BD+43 3213	0.19 ± 0.03	0.23 ± 0.07	−0.18 ± 0.11	0.27 ± 0.07	0.37 ± 0.04	–	0.62 ± 0.37
BD+48 2955	0.22 ± 0.05	0.20 ± 0.03	0.08 ± 0.04	0.30 ± 0.04	0.30 ± 0.07	–	0.23 ± 0.14
HD 174020	0.33 ± 0.03	0.23 ± 0.04	−0.07 ± 0.06	0.29 ± 0.07	0.39 ± 0.03	–	0.26 ± 0.33
HD 174829	0.16 ± 0.04	0.20 ± 0.06	0.05 ± 0.05	0.19 ± 0.03	0.29 ± 0.01	–	0.31 ± 0.04
HD 175740	0.12 ± 0.02	0.07 ± 0.05	−0.05 ± 0.02	0.14 ± 0.03	0.21 ± 0.01	0.30 ± 0.07	0.34 ± 0.03
HD 175884	0.23 ± 0.02	0.20 ± 0.03	−0.01 ± 0.03	0.32 ± 0.03	0.34 ± 0.01	–	0.46 ± 0.06
HD 178797	0.22 ± 0.02	0.32 ± 0.03	0.06 ± 0.03	0.40 ± 0.04	0.42 ± 0.01	0.39 ± 0.22	0.45 ± 0.03
HD 178910	0.20 ± 0.03	0.20 ± 0.03	0.15 ± 0.05	0.20 ± 0.03	0.39 ± 0.04	0.25 ± 0.08	0.36 ± 0.98
HD 179396	0.09 ± 0.02	0.19 ± 0.03	0.04 ± 0.05	0.13 ± 0.02	0.27 ± 0.02	0.31 ± 0.03	0.28 ± 0.04
HD 179959	0.04 ± 0.04	0.06 ± 0.04	0.01 ± 0.03	0.03 ± 0.03	0.15 ± 0.02	–	0.38 ± 0.02
HD 180312	0.09 ± 0.02	0.21 ± 0.03	0.06 ± 0.03	0.09 ± 0.03	0.31 ± 0.01	0.37 ± 0.08	0.19 ± 0.01
HD 180475	0.23 ± 0.03	0.33 ± 0.03	0.03 ± 0.01	0.36 ± 0.04	0.41 ± 0.02	0.30 ± 0.20	0.40 ± 0.03
HD 180658	0.15 ± 0.03	0.19 ± 0.04	−0.01 ± 0.03	0.21 ± 0.03	0.35 ± 0.01	0.21 ± 0.09	0.39 ± 0.04
HD 180682	0.25 ± 0.02	0.45 ± 0.03	0.13 ± 0.02	0.47 ± 0.04	0.51 ± 0.05	0.19 ± 0.05	0.32 ± 0.01
HD 181022	0.34 ± 0.02	0.34 ± 0.06	0.01 ± 0.08	0.49 ± 0.06	–	0.31 ± 0.23	0.09 ± 0.48
HD 181069	0.13 ± 0.02	0.17 ± 0.04	−0.03 ± 0.05	0.19 ± 0.03	0.28 ± 0.02	0.26 ± 0.09	0.45 ± 0.06
HD 181097	0.25 ± 0.02	0.27 ± 0.03	−0.02 ± 0.03	0.35 ± 0.03	0.34 ± 0.02	–	0.46 ± 0.06
HD 181597	0.19 ± 0.02	0.20 ± 0.05	−0.03 ± 0.02	0.27 ± 0.04	0.28 ± 0.00	0.28 ± 0.05	0.42 ± 0.04
HD 181778	0.06 ± 0.03	0.12 ± 0.03	0.00 ± 0.03	0.09 ± 0.03	0.28 ± 0.02	0.47 ± 0.05	0.42 ± 0.12
HD 181880	0.26 ± 0.02	0.30 ± 0.03	0.06 ± 0.04	0.35 ± 0.03	0.42 ± 0.01	–	0.40 ± 0.05
HD 182531	0.22 ± 0.02	0.21 ± 0.05	−0.07 ± 0.03	0.37 ± 0.04	0.39 ± 0.01	–	0.48 ± 0.06
HD 182692	0.19 ± 0.03	0.18 ± 0.04	−0.12 ± 0.03	0.22 ± 0.04	0.35 ± 0.03	0.13 ± 0.05	0.38 ± 0.12
HD 182694	0.10 ± 0.02	0.11 ± 0.04	−0.04 ± 0.02	0.05 ± 0.02	0.14 ± 0.01	–	0.32 ± 0.01
HD 183124	0.17 ± 0.02	0.21 ± 0.04	−0.02 ± 0.04	0.19 ± 0.03	0.29 ± 0.00	0.25 ± 0.05	0.35 ± 0.02
HD 185286	0.34 ± 0.02	0.22 ± 0.04	−0.04 ± 0.04	0.40 ± 0.06	0.42 ± 0.02	–	0.55 ± 0.53
HD 185351	0.13 ± 0.03	0.08 ± 0.05	−0.08 ± 0.02	0.20 ± 0.03	0.22 ± 0.00	0.21 ± 0.09	0.38 ± 0.01
HD 187217	0.16 ± 0.04	0.28 ± 0.02	−0.09 ± 0.03	0.14 ± 0.04	0.32 ± 0.03	0.21 ± 0.14	–
HD 188537	0.11 ± 0.04	0.27 ± 0.04	0.02 ± 0.03	0.11 ± 0.04	0.25 ± 0.05	0.24 ± 0.07	–
HD 188629	0.30 ± 0.03	0.21 ± 0.03	−0.04 ± 0.07	0.37 ± 0.07	0.41 ± 0.04	–	0.46 ± 0.32
HD 188875	0.18 ± 0.04	0.22 ± 0.03	−0.07 ± 0.03	0.29 ± 0.04	0.33 ± 0.02	–	0.61 ± 1.09
HD 226754	0.30 ± 0.02	0.31 ± 0.04	0.03 ± 0.04	0.40 ± 0.06	0.48 ± 0.07	0.43 ± 0.00	0.47 ± 0.18

Section 3.1, and main sequence stars as discussed in Sections 3.2 and 3.3, can be downloaded from the Mikulski Archive for Space Telescopes (MAST) as a High-Level Science Product. TRES spectra are available from somewhere, and all asteroseismic parameters and derived stellar parameters for the red giants in Section 3.1 are provided in an online-only table as Supplementary Material to this paper.

All smear light curves in this paper, as well as the LaTeX source code used to produce this document, can be found at `github.com/benjaminpope/smearcampaign`.

5 CONCLUSIONS

ACKNOWLEDGEMENTS

This work was performed in part under contract with the Jet Propulsion Laboratory (JPL) funded by NASA through the Sagan Fellowship Program executed by the NASA Exoplanet Science Institute. B.P. also acknowledges support from Balliol College and the Clarendon Fund. D.H. acknowledges support by the Australian Research Council's Discovery Projects funding scheme (project number DE140101364) and support by the NASA Grant NNX14AB92G issued through the *Kepler* Participating Scientist Program.

BP acknowledges being on the traditional territory of the Lenape Nations and, today, we recognize that Manhattan continues to be the home to many Algonkian peoples. We thank the Lenape peoples for allowing us to carry out this work on the Lenape original homelands at New York University. BP and TW would like to acknowledge the Gadigal people of the Eora Nation and the Norongerragal and Gweagal peoples of the Tharawal Nation as the traditional owners of the land at the University of Sydney and the Sutherland Shire on which some of this work was carried out, and pay their respects to their knowledge, and their elders past, present and future.

This work has made use of data from the European Space Agency (ESA) mission *Gaia* (`https://www.cosmos.esa.int/gaia`), processed by the *Gaia* Data Processing and Analysis Consortium (DPAC, `https://www.cosmos.esa.int/web/gaia/dpac/consortium`). Funding for the DPAC has been provided by national institutions, in particular the institutions participating in the *Gaia* Multilateral Agreement. This work has in particular made use of the `gaia-kepler.fun` crossmatch database created by Megan Bedell.

Table 5. Chemical abundances relative to iron for stars in the red giant sample as determined by BACCHUS, without differential line-by-line comparison to Arcturus, as described in Section 2.4, for the elements Ni, Mn, Co, Eu, La, Zr, and Sr. Dashes indicate elements for which abundances could not be reliably computed.The catalogue of abundances for more elements continues in Table 6.

Object	[Ni/Fe]	[Mn/Fe]	[Co/Fe]	[Eu/Fe]	[La/Fe]	[Zr/Fe]	[Sr/Fe]
BD+36 3564	0.01 ± 0.04	0.08 ± 0.00	0.13 ± 0.02	0.25 ± 0.03	−0.02 ± 0.07	0.10 ± 0.02	0.34 ± 0.12
BD+39 3577	−0.05 ± 0.03	−0.03 ± 0.06	−0.02 ± 0.02	−0.22 ± 0.04	−0.25 ± 0.02	0.13 ± 0.08	–
BD+43 3064	0.05 ± 0.04	0.21 ± 0.02	0.13 ± 0.02	0.28 ± 0.06	0.15 ± 0.02	0.32 ± 0.04	0.25 ± 0.12
BD+43 3171	0.04 ± 0.05	0.11 ± 0.09	0.14 ± 0.05	0.21 ± 0.05	−0.06 ± 0.11	0.36 ± 0.07	–
BD+43 3213	0.06 ± 0.10	0.33 ± 0.07	0.03 ± 0.05	0.06 ± 0.04	−0.11 ± 0.05	0.49 ± 0.11	0.64 ± 0.47
BD+48 2955	0.05 ± 0.04	0.10 ± 0.02	0.12 ± 0.04	0.28 ± 0.04	0.24 ± 0.05	0.34 ± 0.05	–
HD 174020	0.05 ± 0.05	0.23 ± 0.02	0.10 ± 0.04	0.11 ± 0.04	0.02 ± 0.07	–	0.37 ± 0.89
HD 174829	−0.06 ± 0.04	−0.02 ± 0.07	0.05 ± 0.02	0.15 ± 0.01	0.12 ± 0.05	0.08 ± 0.03	–
HD 175740	0.03 ± 0.04	0.06 ± 0.01	0.08 ± 0.02	0.09 ± 0.07	0.12 ± 0.01	0.18 ± 0.02	–
HD 175884	0.04 ± 0.05	0.14 ± 0.02	0.10 ± 0.02	0.19 ± 0.02	0.14 ± 0.03	0.26 ± 0.02	–
HD 178797	0.05 ± 0.04	0.13 ± 0.11	0.18 ± 0.03	0.26 ± 0.02	0.14 ± 0.02	0.23 ± 0.03	–
HD 178910	0.28 ± 0.07	0.21 ± 0.05	0.17 ± 0.03	−0.02 ± 0.06	−0.13 ± 0.06	0.00 ± 0.03	–
HD 179396	−0.02 ± 0.04	0.09 ± 0.02	0.08 ± 0.03	−0.05 ± 0.03	0.05 ± 0.03	0.04 ± 0.02	–
HD 179959	−0.08 ± 0.04	−0.15 ± 0.04	−0.05 ± 0.02	0.16 ± 0.06	0.18 ± 0.01	0.14 ± 0.07	–
HD 180312	0.02 ± 0.03	−0.09 ± 0.03	0.07 ± 0.01	0.34 ± 0.05	0.04 ± 0.07	0.08 ± 0.02	–
HD 180475	0.03 ± 0.05	0.16 ± 0.04	0.19 ± 0.02	0.19 ± 0.07	0.18 ± 0.03	0.25 ± 0.03	–
HD 180658	0.03 ± 0.06	0.13 ± 0.03	0.11 ± 0.02	–	0.04 ± 0.04	0.16 ± 0.07	–
HD 180682	0.06 ± 0.04	−0.03 ± 0.08	0.20 ± 0.02	0.26 ± 0.03	−0.03 ± 0.02	0.22 ± 0.03	–
HD 181022	0.02 ± 0.07	0.05 ± 0.11	0.14 ± 0.05	0.26 ± 0.03	−0.03 ± 0.21	0.36 ± 0.14	–
HD 181069	0.08 ± 0.05	0.16 ± 0.03	0.12 ± 0.02	0.09 ± 0.03	0.02 ± 0.04	0.10 ± 0.03	–
HD 181097	0.01 ± 0.04	0.02 ± 0.11	0.14 ± 0.03	0.28 ± 0.04	0.17 ± 0.02	0.23 ± 0.03	–
HD 181597	0.03 ± 0.04	0.14 ± 0.01	0.13 ± 0.02	0.18 ± 0.03	0.13 ± 0.01	0.26 ± 0.03	–
HD 181778	−0.00 ± 0.05	0.13 ± 0.02	0.04 ± 0.02	0.16 ± 0.01	0.08 ± 0.03	0.11 ± 0.03	–
HD 181880	0.04 ± 0.04	0.10 ± 0.01	0.18 ± 0.03	0.32 ± 0.04	0.17 ± 0.02	0.33 ± 0.04	–
HD 182531	0.06 ± 0.04	0.17 ± 0.06	0.11 ± 0.02	0.16 ± 0.05	0.15 ± 0.03	0.36 ± 0.03	0.35 ± 0.14
HD 182692	0.03 ± 0.05	0.22 ± 0.02	0.15 ± 0.02	0.01 ± 0.05	0.06 ± 0.04	0.21 ± 0.03	–
HD 182694	−0.07 ± 0.04	−0.08 ± 0.02	0.03 ± 0.03	0.16 ± 0.02	0.16 ± 0.02	0.16 ± 0.04	–
HD 183124	−0.00 ± 0.05	0.01 ± 0.04	0.11 ± 0.02	0.17 ± 0.05	0.04 ± 0.06	0.14 ± 0.04	–
HD 185286	0.12 ± 0.04	0.25 ± 0.01	0.13 ± 0.03	0.18 ± 0.03	0.12 ± 0.05	0.52 ± 0.05	0.30 ± 0.05
HD 185351	0.01 ± 0.04	0.11 ± 0.02	0.15 ± 0.03	−0.06 ± 0.06	0.13 ± 0.03	0.29 ± 0.04	–
HD 187217	−0.03 ± 0.06	−0.10 ± 0.10	−0.03 ± 0.02	–	−0.07 ± 0.03	0.22 ± 0.04	–
HD 188537	0.05 ± 0.07	0.10 ± 0.03	0.12 ± 0.04	0.20 ± 0.04	0.15 ± 0.10	0.30 ± 0.04	–
HD 188629	0.10 ± 0.06	0.22 ± 0.01	0.10 ± 0.02	0.15 ± 0.03	0.06 ± 0.07	0.43 ± 0.01	0.34 ± 0.22
HD 188875	−0.02 ± 0.05	0.23 ± 0.02	0.09 ± 0.03	0.19 ± 0.07	0.20 ± 0.05	0.30 ± 0.03	–
HD 226754	0.19 ± 0.05	0.33 ± 0.03	0.23 ± 0.03	0.28 ± 0.07	−0.05 ± 0.07	0.34 ± 0.04	0.26 ± 0.13

This research made use of NASA's Astrophysics Data System; the SIMBAD database, operated at CDS, Strasbourg, France; the IPython package (Pérez & Granger 2007); SciPy (Jones et al. 2001); and Astropy, a community-developed core Python package for Astronomy (Astropy Collaboration et al. 2013). Some of the data presented in this paper were obtained from the Mikulski Archive for Space Telescopes (MAST). STScI is operated by the Association of Universities for Research in Astronomy, Inc., under NASA contract NAS5-26555. Support for MAST for non-HST data is provided by the NASA Office of Space Science via grant NNX13AC07G and by other grants and contracts. We acknowledge the support of the Group of Eight universities and the German Academic Exchange Service through the Go8 Australia-Germany Joint Research Co-operation Scheme.

REFERENCES

Aigrain S., Parviainen H., Pope B. J. S., 2016, MNRAS, 459, 2408
Alvarez R., Plez B., 1998, A&A, 330, 1109
Ambikasaran S., Foreman-Mackey D., Greengard L., Hogg D. W., O'Neil M., 2015, IEEE Transactions on Pattern Analysis and Machine Intelligence, 38
Angus R., Aigrain S., Foreman-Mackey D., McQuillan A., 2015, MNRAS, 450, 1787
Astropy Collaboration et al., 2013, A&A, 558, A33
Bailer-Jones C. A. L., Rybizki J., Fouesneau M., Mantelet G., Andrae R., 2018, preprint, (arXiv:1804.10121)
Beck P. G., et al., 2011, Science, 332, 205
Beck P. G., et al., 2012, Nature, 481, 55
Bedding T. R., et al., 2011, Nature, 471, 608
Blanco-Cuaresma S., Soubiran C., Jofré P., Heiter U., 2014, A&A, 566, A98
Bodman E., Wright J., Boyajian T., Ellis T., 2018, preprint, (arXiv:1806.08842)
Borucki W. J., et al., 2010, Science, 327, 977
Boyajian T. S., et al., 2016, MNRAS, 457, 3988
Brown T. M., Latham D. W., Everett M. E., Esquerdo G. A., 2011, AJ, 142, 112
Buchhave L. A., et al., 2012, Nature, 486, 375
Campante T. L., et al., 2015, ApJ, 799, 170
Casagrande L., et al., 2014, MNRAS, 439, 2060
Chaplin W. J., Miglio A., 2013, ARA&A, 51, 353
Christiansen J. L., et al., 2012, PASP, 124, 1279
Creevey O. L., et al., 2013, MNRAS, 431, 2419
Creevey O. L., et al., 2015, A&A, 575, A26
Davenport J. R. A., et al., 2018, ApJ, 853, 130
Davies G. R., Miglio A., 2016, Astronomische Nachrichten, 337, 774

Table 6. Chemical abundances relative to iron for stars in the red giant sample as determined by BACCHUS, without differential line-by-line comparison to Arcturus, as described in Section 2.4, for the elements Zn, Y, Cr, V, Cu, and Sc. Dashes indicate elements for which abundances could not be reliably computed.

Object	[Zn/Fe]	[Y/Fe]	[Cr/Fe]	[V/Fe]	[Cu/Fe]	[Sc/Fe]
BD+36 3564	−0.29 ± 0.20	−0.27 ± 0.02	0.23 ± 0.00	0.15 ± 0.03	−0.04 ± 0.06	0.17 ± 0.02
BD+39 3577	−0.24 ± 0.71	−0.40 ± 0.04	0.16 ± 0.10	0.01 ± 0.02	−0.21 ± 0.01	−0.12 ± 0.05
BD+43 3064	–	−0.14 ± 0.05	0.32 ± 0.01	0.24 ± 0.03	−0.16 ± 0.10	0.14 ± 0.02
BD+43 3171	−0.40 ± 0.05	−0.31 ± 0.03	0.29 ± 0.04	0.12 ± 0.06	0.02 ± 0.11	0.14 ± 0.03
BD+43 3213	–	−0.06 ± 0.09	0.39 ± 0.01	0.08 ± 0.09	−0.28 ± 0.11	0.18 ± 0.04
BD+48 2955	–	−0.15 ± 0.05	0.23 ± 0.04	0.20 ± 0.03	−0.05 ± 0.04	0.15 ± 0.03
HD 174020	−0.48 ± 1.11	−0.19 ± 0.06	0.41 ± 0.06	0.26 ± 0.03	−0.20 ± 0.11	0.18 ± 0.03
HD 174829	−0.12 ± 0.13	−0.25 ± 0.06	0.16 ± 0.02	0.01 ± 0.02	−0.23 ± 0.03	0.12 ± 0.03
HD 175740	−0.16 ± 0.16	−0.09 ± 0.07	0.13 ± 0.04	0.09 ± 0.02	−0.16 ± 0.04	0.08 ± 0.03
HD 175884	−0.15 ± 0.17	−0.21 ± 0.07	0.26 ± 0.04	0.21 ± 0.02	−0.10 ± 0.05	0.13 ± 0.02
HD 178797	–	−0.08 ± 0.05	0.26 ± 0.04	0.19 ± 0.02	−0.11 ± 0.04	0.23 ± 0.03
HD 178910	−0.29 ± 0.74	−0.18 ± 0.05	0.29 ± 0.01	0.17 ± 0.02	0.21 ± 0.14	0.14 ± 0.02
HD 179396	−0.07 ± 0.15	−0.27 ± 0.07	0.12 ± 0.03	0.03 ± 0.02	−0.16 ± 0.06	0.10 ± 0.03
HD 179959	0.05 ± 1.84	−0.08 ± 0.06	−0.00 ± 0.03	−0.11 ± 0.02	−0.29 ± 0.05	0.10 ± 0.05
HD 180312	−0.18 ± 0.01	−0.23 ± 0.05	−0.06 ± 0.06	−0.05 ± 0.02	−0.15 ± 0.04	0.15 ± 0.05
HD 180475	−0.09 ± 0.11	−0.25 ± 0.08	0.24 ± 0.04	0.20 ± 0.02	−0.00 ± 0.04	0.21 ± 0.03
HD 180658	0.16 ± 1.25	−0.20 ± 0.01	0.19 ± 0.04	0.15 ± 0.02	−0.05 ± 0.06	0.12 ± 0.03
HD 180682	−0.23 ± 0.14	−0.29 ± 0.04	0.23 ± 0.03	0.26 ± 0.02	−0.06 ± 0.04	0.27 ± 0.02
HD 181022	−0.27 ± 0.03	−0.23 ± 0.02	0.19 ± 0.08	0.10 ± 0.08	−0.01 ± 0.12	0.25 ± 0.04
HD 181069	−0.02 ± 0.19	−0.11 ± 0.08	0.22 ± 0.03	0.15 ± 0.02	−0.10 ± 0.05	0.13 ± 0.03
HD 181097	−0.08 ± 0.41	−0.21 ± 0.03	0.25 ± 0.02	0.19 ± 0.03	−0.12 ± 0.03	0.22 ± 0.03
HD 181597	−0.14 ± 0.15	−0.19 ± 0.08	0.19 ± 0.05	0.21 ± 0.02	−0.18 ± 0.04	0.16 ± 0.02
HD 181778	−0.03 ± 0.18	−0.13 ± 0.04	0.18 ± 0.02	−0.02 ± 0.02	−0.25 ± 0.07	0.05 ± 0.02
HD 181880	−0.04 ± 0.22	−0.20 ± 0.07	0.27 ± 0.03	0.22 ± 0.02	−0.07 ± 0.03	0.23 ± 0.03
HD 182531	0.03 ± 0.78	−0.19 ± 0.07	0.29 ± 0.05	0.24 ± 0.03	−0.08 ± 0.05	0.18 ± 0.02
HD 182692	−0.24 ± 1.34	−0.21 ± 0.10	0.15 ± 0.07	0.24 ± 0.02	−0.11 ± 0.06	0.18 ± 0.03
HD 182694	−0.24 ± 0.07	−0.12 ± 0.05	0.04 ± 0.03	−0.05 ± 0.02	−0.26 ± 0.04	0.09 ± 0.05
HD 183124	−0.18 ± 0.17	−0.24 ± 0.03	0.12 ± 0.04	0.10 ± 0.02	−0.22 ± 0.02	0.10 ± 0.03
HD 185286	–	−0.19 ± 0.08	0.46 ± 0.01	0.34 ± 0.02	−0.11 ± 0.10	0.27 ± 0.03
HD 185351	−0.31 ± 0.10	−0.16 ± 0.05	0.16 ± 0.04	0.18 ± 0.02	−0.17 ± 0.03	0.12 ± 0.04
HD 187217	–	−0.37 ± 0.05	0.28 ± 0.03	0.11 ± 0.03	−0.23 ± 0.02	0.04 ± 0.05
HD 188537	0.32 ± 0.78	−0.27 ± 0.09	0.17 ± 0.01	0.11 ± 0.02	−0.17 ± 0.04	0.06 ± 0.05
HD 188629	–	−0.04 ± 0.10	0.30 ± 0.06	0.31 ± 0.04	−0.15 ± 0.09	0.22 ± 0.04
HD 188875	0.31 ± 1.71	−0.04 ± 0.07	0.33 ± 0.07	0.18 ± 0.02	−0.25 ± 0.07	0.13 ± 0.03
HD 226754	−0.22 ± 1.07	−0.33 ± 0.04	0.38 ± 0.07	0.45 ± 0.04	−0.02 ± 0.07	0.30 ± 0.04

Davies G. R., et al., 2017, A&A, 598, L4
Foreman-Mackey D., Hogg D. W., Morton T. D., 2014, ApJ, 795, 64
Fressin F., et al., 2013, ApJ, 766, 81
Gaia Collaboration et al., 2016, A&A, 595, A1
Gaia Collaboration Brown A. G. A., Vallenari A., Prusti T., de Bruijne J. H. J., Babusiaux C., Bailer-Jones C. A. L., 2018, preprint, (arXiv:1804.09365)
García R. A., et al., 2011, MNRAS, 414, L6
Gilliland R. L., et al., 2010, PASP, 122, 131
Girardi L., 2016, ARA&A, 54, 95
Gustafsson B., Edvardsson B., Eriksson K., Jørgensen U. G., Nordlund Å., Plez B., 2008, A&A, 486, 951
Harvey J., 1985, in Rolfe E., Battrick B., eds, ESA Special Publication Vol. 235, Future Missions in Solar, Heliospheric & Space Plasma Physics.
Hawkins K., et al., 2016a, A&A, 592, A70
Hawkins K., et al., 2016b, A&A, 592, A70
Hawkins K., Masseron T., Jofré P., Gilmore G., Elsworth Y., Hekker S., 2016c, A&A, 594, A43
Hawkins K., Leistedt B., Bovy J., Hogg D. W., 2017, MNRAS, 471, 722
Heiter U., Jofré P., Gustafsson B., Korn A. J., Soubiran C., Thévenin F., 2015, A&A, 582, A49
Hjørringgaard J. G., Silva Aguirre V., White T. R., Huber D., Pope B. J. S., Casagrande L., Justesen A. B., Christensen-Dalsgaard J., 2017, MNRAS, 464, 3713
Huber D., et al., 2012, ApJ, 760, 32
Huber D., et al., 2013, ApJ, 767, 127
Jofré P., 2016, Astronomische Nachrichten, 337, 859
Jofré P., et al., 2014, A&A, 564, A133
Jofré P., et al., 2015, A&A, 582, A81
Jofré P., et al., 2017, A&A, 601, A38
Jones E., Oliphant T., Peterson P., Others 2001, SciPy: Open source scientific tools for Python, http://www.scipy.org/
Kallinger T., et al., 2014, A&A, 570, A41
Kjeldsen H., Bedding T. R., 1995, A&A, 293, 87
Koch D. G., et al., 2010, ApJ, 713, L79
Kolodziejczak J., Caldwell D., 2011, Technical Report 20120003045, Science from Kepler Collateral Data: 150 ksec/year from 13 Million Stars?, http://ntrs.nasa.gov/archive/nasa/casi.ntrs.nasa.gov/20120003045.pdf. NASA Marshall Space Flight Centre, http://ntrs.nasa.gov/archive/nasa/casi.ntrs.nasa.gov/20120003045.pdf
Lindegren L., et al., 2018, preprint, (arXiv:1804.09366)
Lund M. N., et al., 2016, preprint, (arXiv:1612.00436)
Masseron T., et al., 2014, A&A, 571, A47
Masseron T., Merle T., Hawkins K., 2016, BACCHUS: Brussels Automatic Code for Characterizing High accUracy Spectra, Astrophysics Source Code Library (ascl:1605.004), doi:10.20356/C4TG6R
Montet B. T., Simon J. D., 2016, ApJ, 830, L39
Pérez F., Granger B. E., 2007, Computing in Science and Engineering, 9, 21
Petigura E. A., Marcy G. W., 2012, PASP, 124, 1073

Petigura E. A., Howard A. W., Marcy G. W., 2013, Proceedings of the National Academy of Science, 110, 19273
Plez B., 2012, Turbospectrum: Code for spectral synthesis, Astrophysics Source Code Library (ascl:1205.004)
Pope B. J. S., et al., 2016, MNRAS, 455, L36
Ruiz-Dern L., Babusiaux C., Arenou F., Turon C., Lallement R., 2018, A&A, 609, A116
Saio H., Kurtz D. W., Murphy S. J., Antoci V. L., Lee U., 2018, MNRAS, 474, 2774
Schaefer B. E., 2016, ApJ, 822, L34
Silva Aguirre V., et al., 2013, ApJ, 769, 141
Silva Aguirre V., et al., 2015, MNRAS, 452, 2127
Silva Aguirre V., et al., 2016, preprint, (arXiv:1611.08776)
Smith J. C., et al., 2012, PASP, 124, 1000
Stumpe M. C., et al., 2012, PASP, 124, 985
Twicken J. D., Chandrasekaran H., Jenkins J. M., Gunter J. P., Girouard F., Klaus T. C., 2010, in Software and Cyberinfrastructure for Astronomy. p. 77401U, doi:10.1117/12.856798
Van Eylen V., Agentoft C., Lundkvist M. S., Kjeldsen H., Owen J. E., Fulton B. J., Petigura E., Snellen I., 2018, MNRAS, 479, 4786
White T. R., et al., 2013, MNRAS, 433, 1262
White T. R., et al., 2015, in European Physical Journal Web of Conferences. p. 06068, doi:10.1051/epjconf/201510106068
Wright J. T., 2018, Research Notes of the American Astronomical Society, 2, 16
Wyatt M. C., van Lieshout R., Kennedy G. M., Boyajian T. S., 2018, MNRAS, 473, 5286
van Leeuwen F., 2007, A&A, 474, 653
van Saders J. L., Ceillier T., Metcalfe T. S., Silva Aguirre V., Pinsonneault M. H., García R. A., Mathur S., Davies G. R., 2016, Nature, 529, 181

This paper has been typeset from a TEX/LATEX file prepared by the author.